Journal of Energy Storage 78 (2024) 110223

Contents lists available at ScienceDirect

Journal of Energy Storage

journal homepage: www.elsevier.com/locate/est

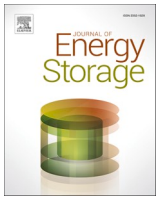

Research Papers

Experimental and numerical analysis of the thermal performance of PCM-impregnated reticular structures obtained by additive manufacturing

Carlo Nonino [a], Luisa Rossetto [b], Andrea Diani [b,*]

[a] Dipartimento Politecnico di Ingegneria e Architettura, Università degli Studi di Udine, Via delle Scienze 206, 33100 Udine, Italy
[b] Dipartimento di Ingegneria Industriale, Università degli Studi di Padova, via Venezia 1, 35131 Padova, Italy

ARTICLE INFO

Keywords:
Paraffin waxes
Reticular structures
Additive manufacturing
Numerical simulations
Stored thermal energy

ABSTRACT

This paper proposes a combined experimental and numerical analysis of the melting of three different paraffin waxes embedded in reticular structures fabricated by additive manufacturing. The parent material of the reticular structures is AlSi10Mg. Metal structures, having a 100 mm square base and a thickness of 20 mm, were printed between two 10 mm thick plates. Samples were positioned in an upright position and laterally heated applying different heat fluxes. Three different paraffins were tested, with different characteristic melting temperatures (42 °C, 55 °C, and 64 °C), which are suitable for electronics cooling applications. Four different structures were tested, having a cell length of 5 mm and 10 mm, and porosities of 0.87 and 0.93. Besides the experimental tests, numerical simulations of the melting phenomenon were carried out using a purely conductive model implemented in ANSYS Fluent. The discretized numerical domains represented just small repetitive portions of the test modules, thus allowing substantial computational time savings. This simplified method has been proven to yield results that are in good agreement with the experimental data. The main outcome of this work is the setup of the simplified numerical procedure, which was then validated and used to investigate the effectiveness of the considered structures in diffusing heat into the low thermal conductivity phase change materials. It was concluded that the best overall thermal performance can be obtained with low porosity and low cell size since this enables faster melting processes and better surface temperature control.

1. Introduction

Phase Change Materials (PCMs) are a class of materials used to benefit from the thermal energy that is stored (or released) when a phase transition from solid to liquid (or vice versa) occurs. PCMs are available in a broad range of melting temperatures, making them suitable for a wide range of applications, such as cooling, heating, or power generation. Their main drawback is the low thermal conductivity, and this is the reason why PCMs are often coupled with a metallic matrix aimed at enhancing the overall thermal conductivity. This metal structure may be made up of fins, may be a foam with stochastically organized open pores, or a honeycomb, composed of repeating elementary open cells.

Nowadays, the actual additive manufacturing (AM) technology is not limited to polymeric materials to be printed, but also includes metallic materials, thus opening new frontiers for heat transfer devices. Many single-phase applications have been considered in existing studies [1–5], whereas only a few studies on possible solid media fabricated using AM for applications related to PCMs have been conducted [6–11]. AM allows the manufacturing of a high variety of geometries of metal matrices, with no constraints on the porosity of the printed matrix. It enables complex structures that would not have been possible with standard manufacturing methods. Metals such as copper, aluminum, titanium alloys and stainless steel can be used in the printing process [11]. Besides this, since the metal matrix is printed on the heated/cooled surface, no contact thermal resistance between the structure and the heated or cooled plate is present.

Embedding the metal matrix in the PCM increases the thermal conductivity of the composite structure with respect to a solution with only pure PCM, shortens the melting time of the PCM, allows a more uniform temperature distribution in the PCM, decreases the maximum temperature difference, and improves the energy storage rate [11].

Applications of these composite structures (PCM plus AM metallic matrix) span from thermal management of power battery packs [12] to lightweight heat storage for passive cooling applications in modern aircrafts [13]. They can be applied as thermal dampers to optical instruments for aerospace applications [14]. The composite units can also

* Corresponding author.
E-mail address: andrea.diani@unipd.it (A. Diani).

https://doi.org/10.1016/j.est.2023.110223
Received 18 July 2023; Received in revised form 12 December 2023; Accepted 19 December 2023
Available online 2 January 2024

be used for automotive applications, to recover, store, and re-use the waste heat from the engine cooling system to speed up the cold-start phase, which is critical for the production of pollutants [9].

While numerical studies are available in the literature, such as the works carried out by Qureshi et al. [15,16], only a few experimental studies on periodic solid structures with PCM are available, thus more data are needed. This study presents new experimental results concerning the solid-liquid phase change of organic PCMs, in this case, paraffins embedded in reticular structures fabricated by AM. Four metal lattices, composed of repeating cubic cells, with different porosity and cell size and three types of paraffin with different melting temperatures (42 °C, 55 °C, 64 °C) were tested by applying different heat fluxes (10, 15, and 20 kW m^{-2}). Moreover, a simplified numerical model, validated through comparison with the experimental data of this study, is presented. This simplified numerical method allows accurate simulations of thermal transients in the test modules using reduced computational domains, combined with an original model of the effects of the thermal capacity associated with the lateral insulating structures and of the heat losses at the corresponding external surfaces.

The validated numerical procedure is then used to analyze the thermal performance of the same reticular structures and paraffins considered in the experiments, but with reference to applications under imposed specific heat flux and under constant temperature boundary conditions, for thermal control of intermittently operating devices or for devices involving thermal energy storage.

The organization of the paper is as follows: Section 2 reports information about the metal structures, paraffins, and test modules laterally heated by the Joule effect. Section 3 reports the experimental results. The numerical model is described in Section 4. Section 5 is dedicated to the numerical results, with an analysis of grid and time step in Section 5.1, comparisons between the numerical simulations and experimental data in Section 5.2, and an assessment of the effectiveness of the different metal matrices for the diffusion of heat in the PCM in Section 5.3 and in Section 5.4, where constant heat flux and constant wall temperature boundary conditions are considered. Section 6 finally presents the conclusions.

2. Experimental apparatus

2.1. Reticular structures

The base cells of the considered reticular structures are cubic cells as those shown in Fig. 1. Two different cell sizes were considered (5 mm and 10 mm), each one with two different porosities (87% and 93%). These structures will be named RET5-87, RET5-93, RET10-87, and RET10-93, where the first number denotes the cell size, while the last number denotes the porosity. Table 1 reports the main geometrical parameters of the metal lattices. The samples were made by the repetition of the base cell, in order to create the periodic structures which embed the phase change material. These periodic structures were 3D printed between two plates (100 × 100 × 10 mm^3), thus, no thermal resistance existed between the plates and the structure. The thickness of the reticular structure is 20 mm. Fig. 2 shows two of the printed reticular structures with the two plates. The parent material is an aluminum alloy (AlSi10Mg) with a thermal conductivity of 175 W m^{-1} K^{-1}, a specific heat of 900 J kg^{-1} K^{-1}, and a density of 2670 kg m^{-3}. The structures were fabricated by LAMA FVG lab (Udine, Italy) using selective laser melting, which is an AM technique. This technique allows the construction of metal components starting from CAD files by selectively fusing metal powders layer after layer until the entire object is created.

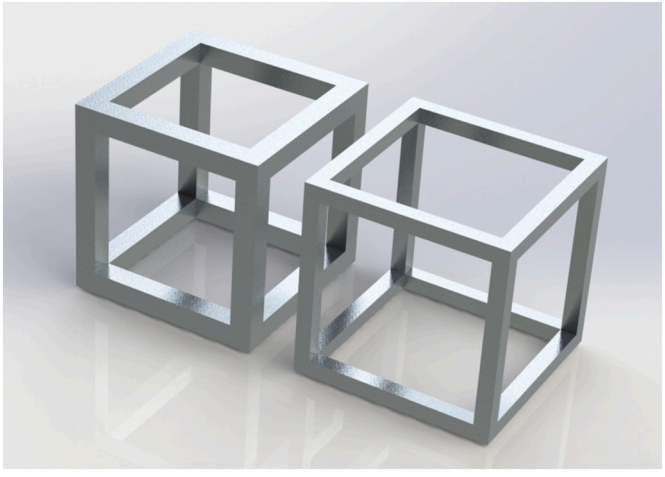

Fig. 1. Base cells of reticular structures: 87% porosity (left), and 93% porosity (right), with the same cell size.

The two plates contain calibrated home-made T-type thermocouples (accuracy of ±0.1 K), to monitor the wall temperature during the heating process. The location of these thermocouples can be highlighted in the bottom section of Fig. 2.

2.2. Test module

The entire structure is tested in an upright position, and it is laterally heated by means of a homemade copper heater inside which a guide was milled to host a nickel-chrome wire resistance. A high thermal conductive paste was used to fill the air gaps between the wire and the guide. The electrical resistance is connected to a DC power supplier (ALN 30.30 series by CEA srl). Three different heat fluxes were applied: 10, 15, and 20 kW m^{-2}, which correspond to heat flow rates of 100, 150, and 200 W. The heat flow rate was calculated as the product between the electrical differential potential (EDP) across the electric heater and the current flowing into the circuit. The current was measured with a reference resistance (planar shunt 32 A by LEM International SA). From the knowledge of the value of the calibrated reference resistance, by measuring the electrical differential potential at the shunt and applying Ohm's law, it is possible to derive the value of the current flowing in the electrical heater. The electric power was thus measured with an uncertainty of ±0.13% of the reading.

A schematic of the test module is reported in Fig. 3. Two bakelite plates cover the bottom and rear side of the sandwich-like structure, whereas a glass window is positioned on the front side, to permit the visualization of the melting front of the PCM melting inside. The entire structure is inserted in a Teflon housing, to limit the heat losses to the ambient as much as possible. Three holes were drilled on the lateral side opposite the heated side to host three T-type thermocouples whose tips measure the temperature of the PCM in the centerline of the periodic structure with an accuracy of ±0.5 K. These three thermocouples are located in the centerline at 2.5, 5.0, and 7.5 cm from the bottom side of the periodic structure, i.e., they measure the temperature of the phase change material at three different heights. All the implemented thermocouples are connected to an ice point reference (K170—50C by Kaye Thermometrics Inc). The top part is not covered to permit the filling of the periodic structure with the paraffins.

All the signals are connected to the data acquisition system, which is a National Instruments CompactDAQ 9178 USB chassis with NI-9213

Table 1
Geometrical characteristics of the tested structures.

Property	RET5-87	RET5-93	RET10-87	RET10-93
Cell size [mm]	5	5	10	10
Porosity [%]	87	93	87	93
Fiber thickness [mm]	0.565	0.4	1.13	0.8
Heat transfer area/volume [m^2 m^{-3}]	420	323	210	161

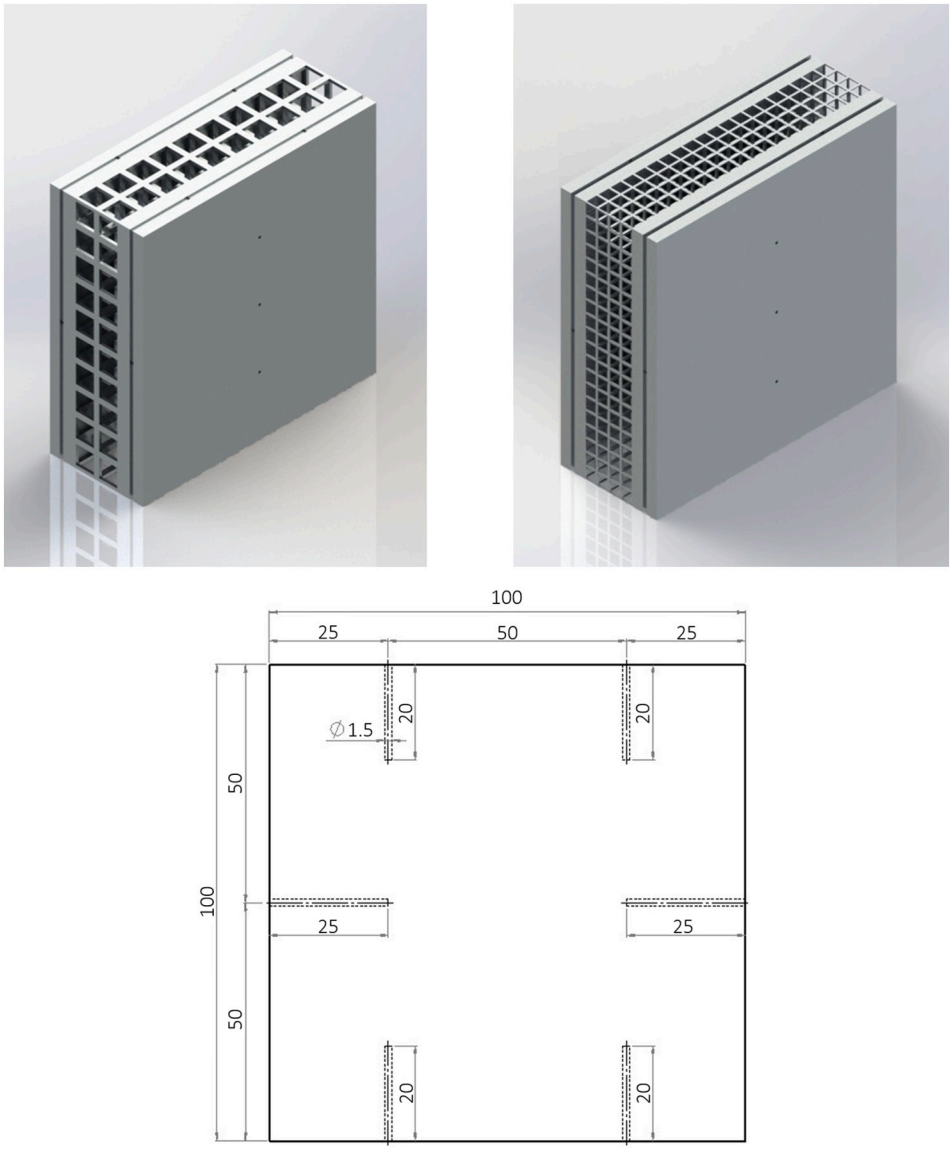

Fig. 2. Examples of reticular structures: RET10-87 (top-left) and RET5-93 (top-right) and locations of holes for thermocouples in the left-side (heated) plate (bottom). Dimensions expressed in [mm].

Fig. 3. Assembled test module (RET10-93).

modules for thermocouples and a NI-9219 universal module for the voltage measurements at the shunt as well as at the electric heater. During the experimental tests, the data acquisition system is tuned at 1 Hz as the sampling rate.

2.3. Paraffin waxes

Three different paraffin waxes were tested: RT42, RT55, and RT64HC manufactured by Rubitherm Technologies GmBH [17]. The number that appears in the name of each paraffin represents the characteristic melting temperature, even if it is better to consider a melting temperature range instead of a single temperature, as reported in Table 2 together with the main thermophysical properties of the tested paraffins, which are chemically inert, with a stable performance after multiple phase change cycles.

3. Experimental results

Each reticular structure was tested with three different paraffin waxes, each one with three different heat fluxes. The purpose was to

Table 2
Thermophysical properties of the tested paraffins. Data from the manufacturer [17].

Property	RT42	RT55	RT64HC	
Melting temperature range	38–43	51–57	63–65	[°C]
Heat storage capacity[a]	165	170	250	[kJ kg^{-1}]
Specific heat capacity	2	2	2	[kJ kg^{-1} K^{-1}]
Solid density[b]	0.88	0.88	0.88	[kg dm^{-3}]
Liquid density[c]	0.76	0.77	0.78	[kg dm^{-3}]
Thermal conductivity	0.2	0.2	0.2	[W m^{-1} K^{-1}]
Volume expansion	12.5	14	11	[%]

[a] Combination of latent and sensible heat in a temperature range of 35 and 50 °C for RT42, of 48 and 63 °C for RT55, of 57 and 72 °C for RT64HC.
[b] Evaluated at 15 °C for RT42 and RT55, at 20 °C for RT64HC.
[c] Evaluated at 80 °C.

generate a dataset sufficient not only to have some insights into the physics of the studied phenomena but also to allow the validation of a simplified numerical model aimed at extending the experimental results for a better characterization of the thermal performance of the considered structures. The test modules were filled with the PCM in the liquid phase, and this procedure was deemed concluded once the liquid paraffin filled the entire structure. After filling, the modules were allowed to cool down to ambient temperature, i.e., the experimental tests started at room temperature. Considering all the experimental melting tests, the ambient temperature varied from 17.3 °C to 28.1 °C. Due to the volume contraction from liquid to solid state, the solid paraffin did not fill the entire structure: this choice was taken to prevent liquid leakage during the melting process. The data acquisition system (DAQ) was switched on as soon as the DC power supplier was turned on, and the DAQ was set with a frequency of 1 Hz. Each experimental test was deemed concluded as soon as all the PCM was completely melted inside the periodic structure. The temperature of the heated side, as well as the temperatures of the PCM, were recorded.

With reference to the heating process with an applied heat flux of 10 kW m^{-2} and all the structures and paraffin waxes considered, Fig. 4 shows the time-temperature profiles recorded by the thermocouples embedded in the heating plate (T_{heat}) (average value among the six recorded values) and by the three thermocouples located in the centerline at 2.5, 5.0, and 7.5 cm from the bottom (T_{bot}, T_{mid}, and T_{top}, respectively). The curve of T_{top} for the case (RET5-93, RT42) is omitted because the corresponding thermocouple gave unreliable readings. The temperature of the heated side increases almost linearly when only sensible heat is involved in the heating process. Then the slope of the curve decreases when the lower limit of the melting temperature range of the PCM is reached, i.e., also latent heat becomes involved. The curves pertaining to the temperatures of the PCM in the midplane, instead, present two changes of slope: the first one is in correspondence to the lower value of the melting temperature range, whereas the second one is in correspondence to the upper value of the melting temperature range. It is apparent that in most cases the temperature profiles detected by thermocouples placed at different heights within each test sample are very close to each other and almost overlap for large parts of the transients. This means that the melting front is almost vertical, at least up to the midplane, and that, in general, the effects of natural convection on the thermal field in the PCM are not very pronounced. Some significant separation between the curves only appears in the cases (RET10-93, RT42) and (RET10-93, RT55), i.e., those corresponding to the combination of coarser metal matrix, higher porosity, and lower melting point paraffins. The effects of convective motions, on the other hand, are completely negligible in the case of the 5 mm structure and 87% porosity and still modest even with the 10 mm cells and the same porosity. This is consistent with the findings of Lafdi et al. [18], who carried out experiments similar to those described in this paper, but using metal foams, and concluded that, with a porosity of 88.4% or less, the convective motions in the PCM were negligible. The trend shown here is also in line with the results of Paek et al. [19], who had shown that, for a fixed porosity, the permeability of the structure increased as the pore size increased. From a physical point of view, this can be explained by considering that, in the case of composite structures such as those analyzed in this work, consisting of a metal matrix with high thermal conductivity impregnated with PCM, the presence of the ligaments forming the cells not only results in a high flow resistance that has the effect of strongly impeding convective motions but also has the effect of homogenizing the temperature within the structure itself with a consequent reduction in the local density differences responsible for convective motions. In addition, it can be noted that the small size of the elements of the cellular structures implies low values of the Grashof number, which is proportional to the characteristic length cubed. Moderate values of this dimensionless parameter are normally associated with reduced natural convection effects. It can thus be concluded that the heat transfer mechanism is dominated by conduction [20,21]. Based on the above observations, it was deemed reasonable to consider a purely conductive numerical model to study the effectiveness of different metal matrices for heat diffusion within a phase-change material. Moreover, any convective motions in the PCM would be strongly influenced not only by the pore size, but also by the overall geometry of the composite structure, and that would make it impossible to draw conclusions of general validity, while the main purpose of this work is to validate a model that allows the comparison of different structures with respect to their ability to diffuse heat within the PCM. Experimental results like those shown in Fig. 4 were also obtained with applied heat fluxes of 15 kW m^{-2} and 20 kW m^{-2}, but they are not reported here for the sake of brevity. However, all the experimental results were used for the validation of the numerical model described below.

4. Numerical model

The commercial finite volume code ANSYS Fluent [22] was employed to perform numerical simulations aimed at demonstrating the validity of a simplified, purely conductive model previously developed for the analysis of the thermal field inside test modules like those considered in the present experiments, but with the metallic structure that, instead of being reticular, consisted of Body Centered Cubic (BCC) cells [23]. The obvious advantage of such a model is that, when it can be applied, i.e., when natural convection effects are negligible, a pore-scale parametric analysis can be carried out with reference to a reduced computational domain and without the need to solve the Navier-Stokes equations, resulting in huge savings in computer time. The phase change process analyzed here is governed by the nonlinear transient heat conduction equation

$$\frac{\partial(\rho c T)}{\partial t} = \nabla\cdot(k\nabla T) + \dot{q} \tag{1}$$

where T is the temperature, t is the time, ρ, c, and k are the density, specific heat capacity, and thermal conductivity, respectively, and $\dot{q}$ is the volumetric heat generation. The latent heat storage/release process is accounted for by assuming $c = c_{app}$ for the PCM, where $c_{app} = \partial h_{PCM}/\partial T$ is an apparent specific heat capacity and h_{PCM} is the enthalpy per unit mass of the PCM [24].

$$h_{PCM} = \int_{T_{ref}}^{T} \left[c_{PCM} + L_{PCM}\frac{\partial \beta}{\partial T} \right] \mathrm{d}T \tag{2}$$

The meaning of symbols is the following: c_{PCM} and L_{PCM} are the specific heat capacity and latent heat of phase change of the PCM, respectively; β represents the liquid fraction during the melting process; T_{ref} is the reference temperature. In the numerical solution of Eq. (1), the use of the apparent specific heat of the PCM, which is a function of temperature, allows accounting for the latent heat of phase change. The enthalpy-temperature curves and the corresponding apparent specific heat-temperature curves for the three paraffinic waxes considered in this

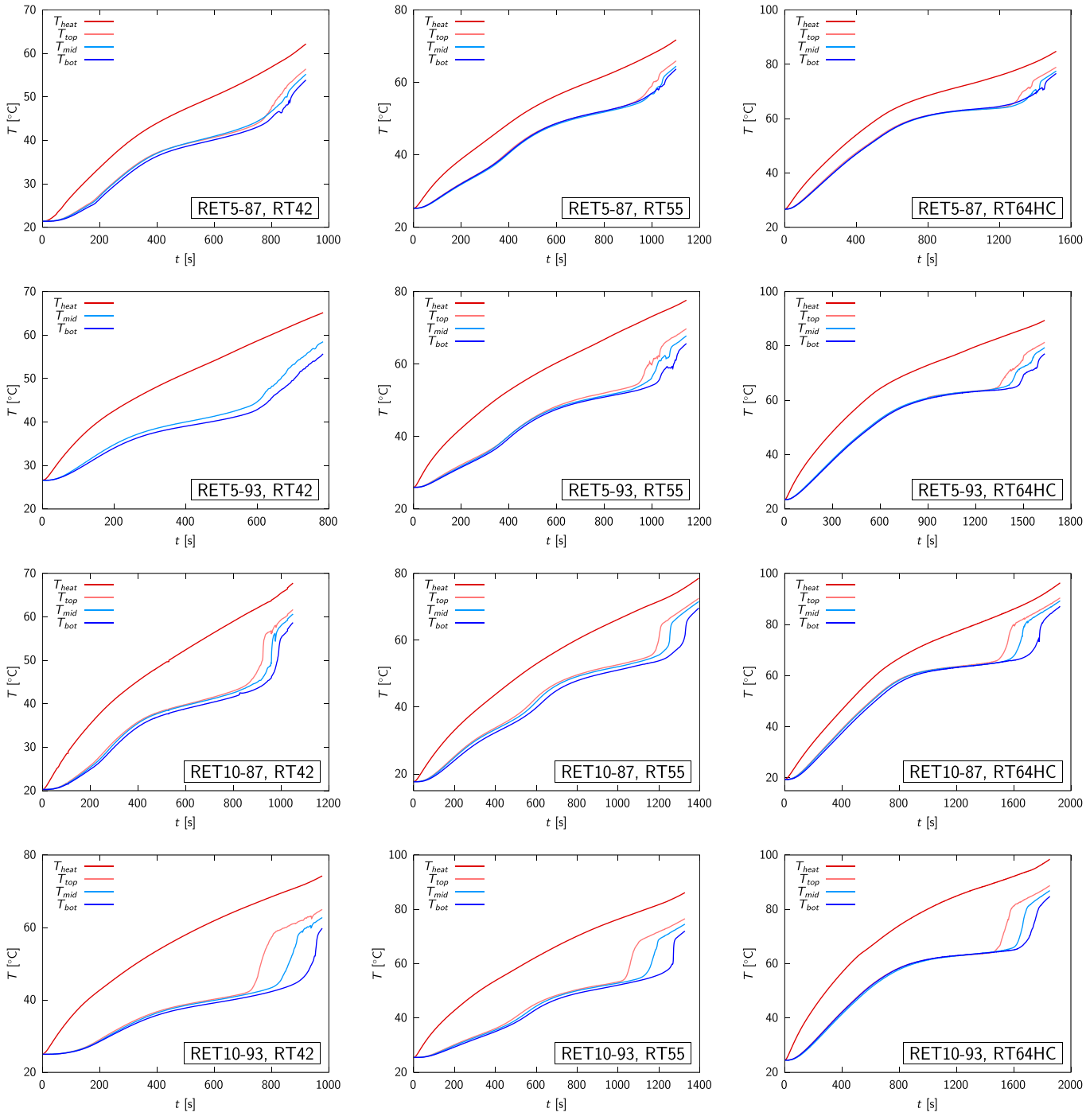

Fig. 4. Time-temperature profiles with an applied heat flux of 10 kW m^{-2} and all the reticular structures and paraffin waxes considered.

work are shown in Fig. 5. The piecewise linear functions provided as input to the ANSYS Fluent software for the numerical simulations were based on the manufacturer's data [17]. As can be seen in Fig. 5, in the case of the paraffin waxes considered, the enthalpy does not vary linearly within the melting temperature range. It must be emphasized that the above method represents a better alternative to the one integrated into the ANSYS Fluent code, which only allows a linear variation of the enthalpy within the phase change temperature range.

Due to existing symmetries, reduced computational domains such as those shown in Fig. 6, corresponding to one-fourth of repetitive units inside the test modules, can be used to study the transient thermal fields in the composite structures consisting of the PCM-impregnated metal matrices. The heater was modelled as a 4 mm thick nickel-chrome layer with internal heat generations of 2.5, 3.25, and 5.0 MW m^{-3}, corresponding to the heat fluxes of 10, 15, and 20 kW m^{-2}. Despite the presence of the thermal insulation enclosing the test module, there were some heat losses to the environment at the side surfaces of the module itself. These had an influence on the recorded thermal transients, but cannot be modelled directly if, as in this case, a reduced computational domain is considered for the analysis. Therefore, to account for the effects of the heat losses on the experimental results, convention boundary conditions

$$q^{'} = \alpha_{eq}(T_{amb} - T_s) \tag{3}$$

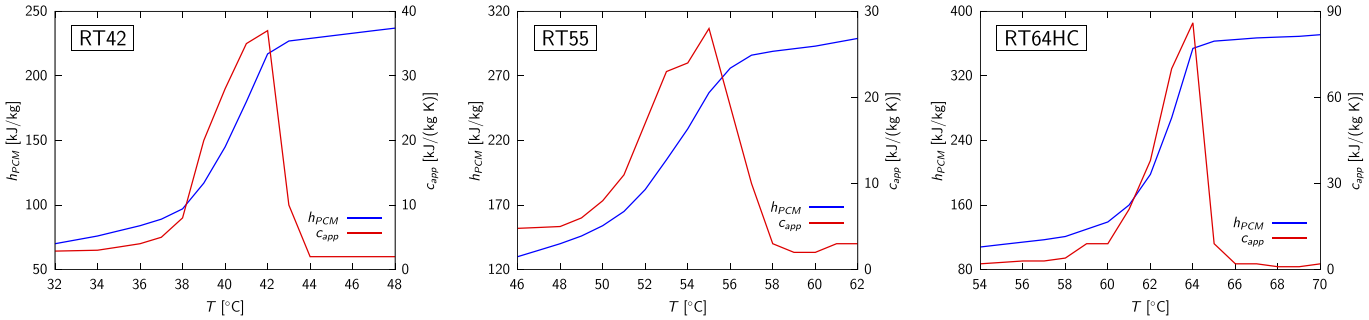

Fig. 5. Enthalpy-temperature curves and corresponding apparent specific heat-temperature curves for the three paraffin waxes considered ($h_{PCM}(T_{ref}) = 0$ kJ kg^{-1} at $T_{ref} = 0$ °C).

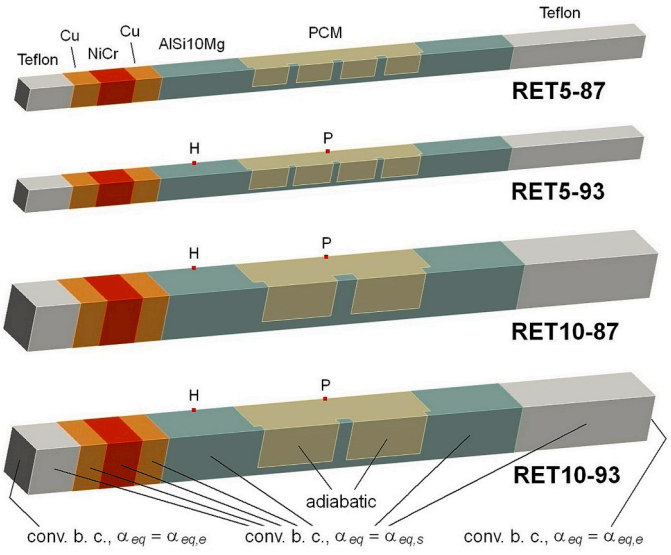

Fig. 6. Computational domains and imposed boundary conditions.

were applied on the entire lateral surface of the computational domain, including those that should be adiabatic because of symmetry. In the above equation, q'' is the heat flux associated with thermal losses, T_{amb} is the room temperature, T_s is the temperature of the boundary of the computational domain, and α_{eq} is an equivalent convection coefficient. Values of α_{eq} equal to $\alpha_{eq,s} = 0.25$ and 0.50 W m^{-2} K^{-1} were selected for the symmetry surfaces of RET5 and RET10 structures, respectively, with the exclusion of those belonging to the PCM to avoid distortion of temperature profiles. For the external surfaces of the Teflon layer, α_{eq} was assumed equal to $\alpha_{eq,e} = 10$ W m^{-2} K^{-1}. The heat capacity of the insulating structures on the sides of the test modules was accounted for with a fictitious 50% increase in the density of the Teflon layer. To mimic the experimental conditions, contact resistances of 0.001 K m^2 W^{-1} and 0.0001 K m^2 W^{-1} were added between the nickel-chrome and copper layers, and at the copper-AlSi10Mg interface, respectively.

The thermophysical properties of the paraffin waxes, which were used to specify a piecewise linear variation of c_{app} with temperature, are reported in Table 2, while those of the solid materials are listed in Table 3.

Table 3
Thermophysical properties of solid materials.

Property	AlSi10Mg	Cu	NiCr	Teflon
Specific heat capacity [J kg^{-1} K^{-1}]	871	381	440	1300
Thermal conductivity [W m^{-1} K^{-1}]	175	387.6	60	0.3
Density [kg m^{-3}]	2719	8978	8900	2200

5. Numerical results

5.1. Grid and time step independence tests

The computational domains were discretized using a mixture of hexahedral and tetrahedral cells, the least square cell-based method was used for gradient calculations, equilibrium temperature conditions of wax and solid at the interfaces between the two materials were assumed, and an implicit second-order method was used for time integration. Up to 25 iterations were required within each time step, with an absolute tolerance on the residuals set at 10^{-9}. Grid independence tests were conducted with reference to the RET10-87 structure, the RT55 paraffin, heat flux at the heater $HF = 10$ kW m^{-2}, and an initial temperature of 17.7 °C. The temperature-time evolutions at two points within the domain were monitored, namely, a point located on the heated slab corresponding to point H in Fig. 6 and one on the mid-plane of the PCM layer corresponding to point P in the same figure.

Based on preliminary tests, a grid had been selected with cell sizes smaller than or equal to 0.6 mm in the solid layers and 0.3 mm in the parts of the domain corresponding to the PCM and the metal matrix, with a total number of cells equal to 317,057. In addition, a time step Δt equal to 7 s was chosen by dividing the transient into about 200 time intervals. To verify that the solution was nearly independent of the time step and grid size, the simulations were also repeated with a time step doubled or halved, i.e., 14 s or 3.5 s, and then also using a coarser grid and a finer grid, with cells having maximum sizes increased or decreased by a factor of 1.5 from those initially chosen.

Fig. 7 (left) shows the time trends of temperatures at point H and point P, obtained with different combinations of grid resolution and time step corresponding to cases A (reference case), B, C, D, and E identified in Table 4. Despite significant variations in grid size and time step between cases, the curves are all overlapping, and only in case B (time step doubled) there are small discrepancies, as shown in the inset. The black curve, pertaining to the reference case (A), cannot be seen because it is completely hidden by the other curves. The results of further comparisons are shown in Table 4 where, in addition to the temperatures T_H and T_P at points H and P at the simulation time $t = 1000$ s, the corresponding percentage differences

$$\%\Delta T = 100\frac{T - T_{sel}}{T_{sel} - T_{init}} \tag{4}$$

are reported. They are calculated with reference to the values obtained in the different cases and those for the selected combination of grid and time step, which are chosen as reference and shown in bold print in the table. In the previous equation, T_{sel} is the temperature computed with the selected grid and/or time step, and T_{init} is the initial temperature. It is apparent in Table 4 that even with significant variations in the time step and grid size and, therefore, in the number of cells, the temperature differences between cases never exceed ±0.08 K, with $\%\Delta T$ always remaining well below ±0.2 %. Therefore, based on these comparisons,

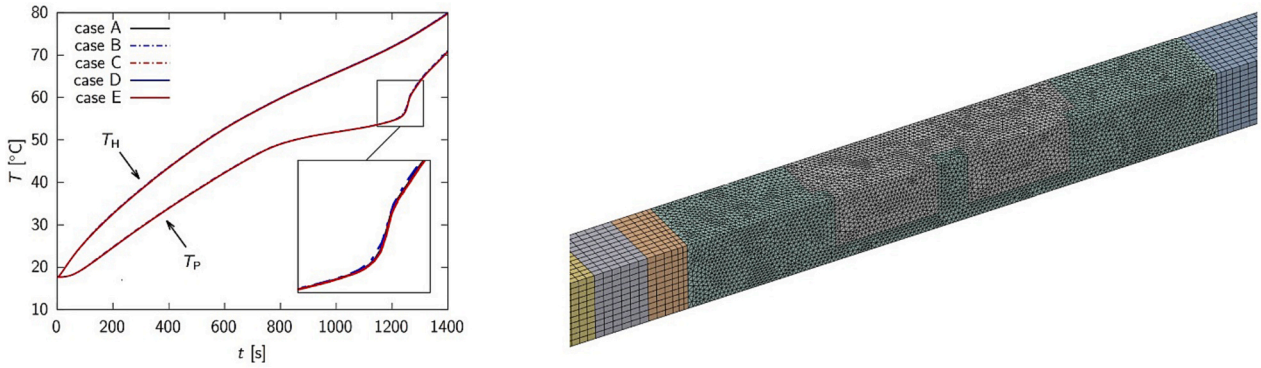

Fig. 7. Grid and time step independence tests: time trends of temperatures at point H and point P for the test cases considered (left); detail of the selected grid for the RET10-87 structure (right).

Table 4
Grid and time step independence tests: temperatures and percentage temperature differences at time $t = 1000$ s (boldface: reference grid and time step).

Case	N. cells	Δt [s]	T_H [°C]	$\%\Delta T_H$	T_P [°C]	$\%\Delta T_P$
A	**317,057**	**7.0**	**65.820**	**0.000**	**51.852**	**0.000**
B	317,057	14.0	65.897	0.162	51.882	0.088
C	317,057	3.5	65.780	−0.083	51.837	−0.043
D	95,094	7.0	65.873	0.111	51.849	−0.008
E	1,063,434	7.0	65.744	−0.158	51.843	−0.028

the results can be considered nearly time step and grid independent. As an example, a detail of the grid used for the simulations concerning the RET10-87 structure is shown in Fig. 7 (right). The same maximum cell sizes were also adopted to discretize the RET10-93 structure, while in the case of the RET5-87 and RET5-93 structures, these dimensions were reduced to 0.4 mm and 0.2 mm, respectively. Thus, grids with 262,819, 266,904, 317,057, and 315,499 cells were used for the numerical simulations concerning RET5-87, RET5-93, RET10-87, and RET10-93, respectively. Regarding the time steps used in the other simulations, based on the previously mentioned criterion of dividing the transients into about 200 time intervals, values of the time step ranging from 3 s to 9 s were chosen in the different cases.

5.2. Validation

To validate the numerical model, comparisons were made between the results of the numerical simulations and the data collected during the experimental tests for the RET5-87, RET5-93, RET10-87, and RET10-93 structures and all the paraffins and heat fluxes considered. Fig. 8 shows the trends in time of the temperature $T_{P,NUM}$ of the reference point (point P in Fig. 6), which is compared with the temperature $T_{ave,EXP}$, average of the temperatures measured experimentally by the three thermocouples placed in the PCM layer. In fact, it was deemed reasonable to consider $T_{ave,EXP}$ as the most representative temperature of that on the median plane in the PCM to compare with the one yielded by the numerical simulations, which only refers to a single point of a repetitive unit within the test module. The time-temperature profiles of the heated plate at the point corresponding to that where the thermocouples were placed (point H in Fig. 6), are also compared with the corresponding experimental data ($T_{H,NUM}$ and $T_{heat,EXP}$, respectively). As already mentioned, since the initial temperatures (equal to the ambient temperatures T_{amb}) were different in the different tests, ranging from 17.3 °C to 28.1 °C, the excess temperature $T - T_{amb}$ is reported on the vertical axes of the graphs. As can be seen, even though the specific heat capacities and the thermal conductivities of the solid and liquid phases of the PCM are only known with an accuracy of one significant digit, the agreement between numerical and experimental data is more than satisfactory in all cases, with the deviations being the largest for the RET5-93 structure, but still acceptable. Therefore, it can be concluded that the proposed numerical model can capture the main thermal effects produced by the different metal matrices on the phenomena related to the storage and release of latent heat of phase change in the test modules.

5.3. Thermal performances of reticular structures

The experimental results were instrumental for the validation of the numerical model, but they did not allow an accurate assessment of the effectiveness of the different metal matrices for the diffusion of heat in the PCM because the initial and ambient temperatures during the tests were not always the same, and this affected the duration of the transients. Therefore, to easily compare the thermal performance of the different structures, the numerical simulations for the case of applied heat flux $HF = 10$ kW m^{-2} were repeated always using the same value of 20 °C for the initial and ambient temperatures. Moreover, to obtain results that were not influenced by the finite size of the test module, the convection coefficient α_{eq} in Eq. (3) was assumed equal to zero on the lateral boundaries. The time-temperature profiles for the same points H and P considered earlier are shown in Fig. 9 for all the structures and paraffin waxes. It is clearly seen that the reticular structure with the lowest porosity and smallest cell size (RET5-87) is the one that allows for faster phase change processes and a lower heated surface temperature than all others. A slightly lower performance in controlling the temperature of the heated surface is provided by the RET10-87 structure. However, point P on the midplane remains at a lower temperature for a longer period of time than in the cases where the cell size is 5 mm because it is located at a greater distance from the metal structure. Finally, the RET10-93 structure, characterized by low porosity and larger cell size, is the one that determines the longest times for the phase change process and the highest values of the heated surface temperature.

5.4. Further thermal performance analyses

The analysis of the thermal performance of the structures was then completed by considering the case where the metal plates are 1 mm thick, rather than 10 mm thick, to minimize the effect of their heat capacity on thermal transients, which are thus affected almost solely by the characteristics of the metal matrix and PCM. The structures considered for this part of the analysis are shown in Fig. 10, but, as before, the computational domain for the numerical simulations only included one repetitive unit of the PCM-impregnated metal matrix. The convection coefficient α_{eq} on the lateral boundaries was assumed to be zero to simulate a structure infinitely extended laterally; in addition, the surface opposite the heated surface was also assumed to be adiabatic. To better characterize the thermal behavior of the structures with reference

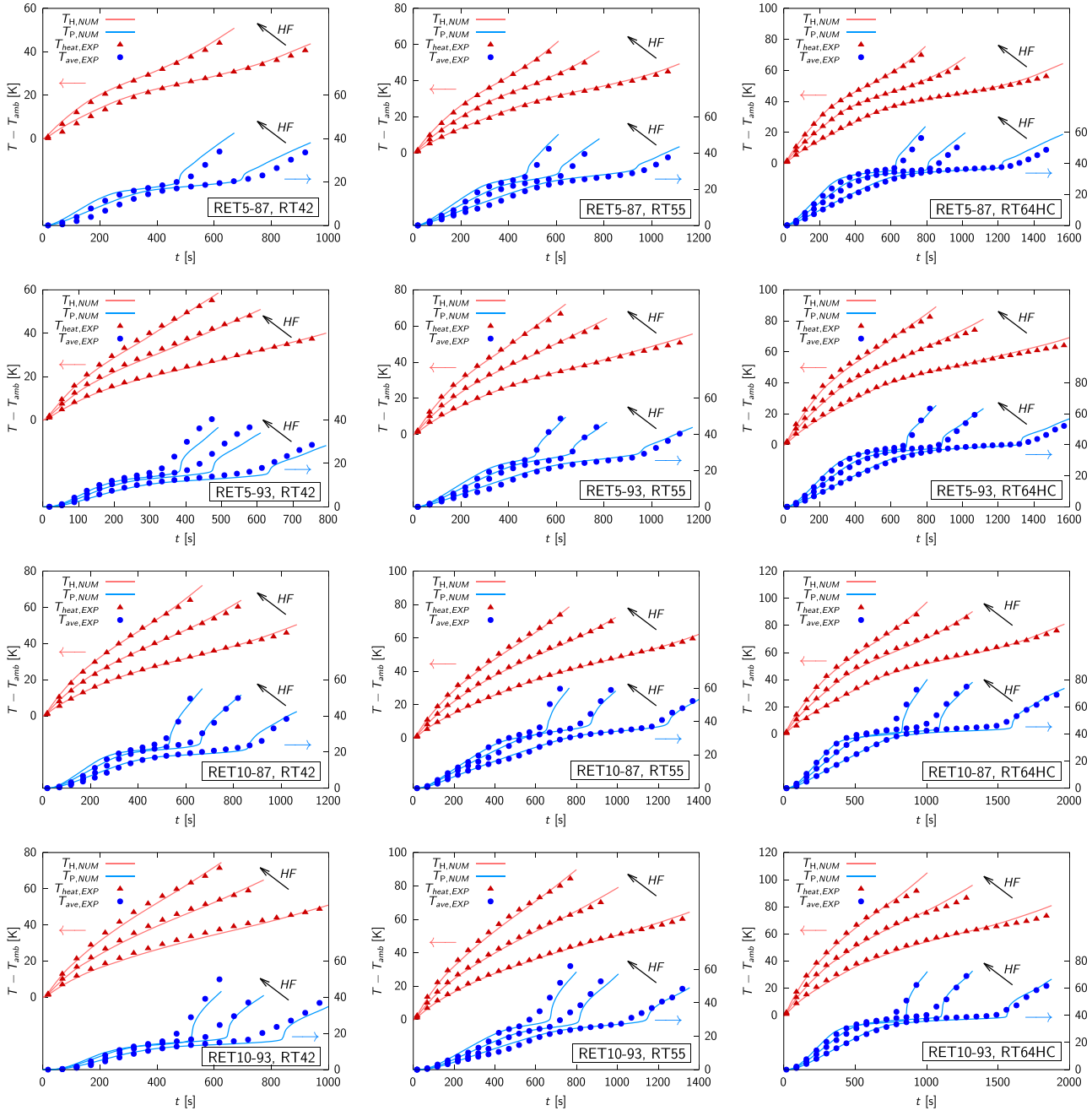

Fig. 8. Comparisons of numerical (solid curves) and experimental (symbols) time-temperature histories for the RET5 and RET10 structures (applied heat flux *HF* equal to 10, 15, and 20 kW m^{-2}).

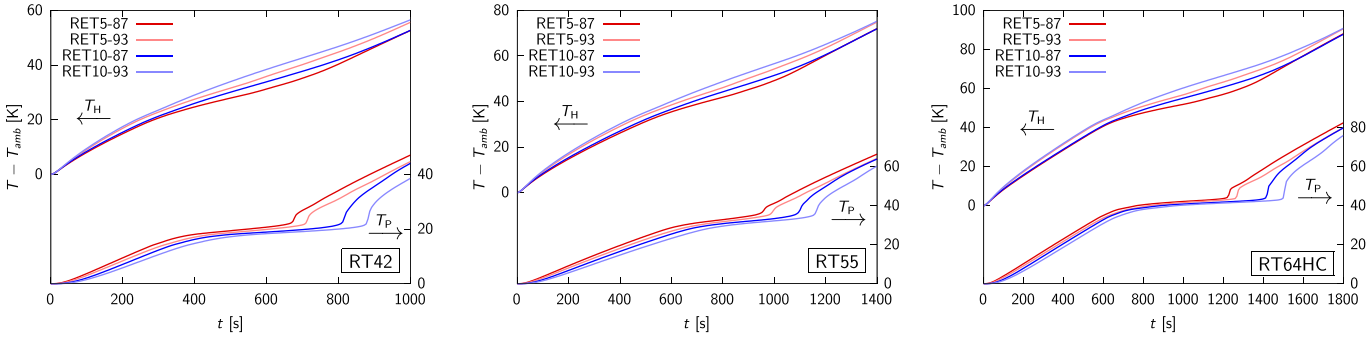

Fig. 9. Points H and P: time-temperature profiles for all the structures and PCMs, heat flux $HF = 10$ kW m^{-2}, $T_{init} = T_{amb} = 20°C$ and adiabatic lateral boundaries.

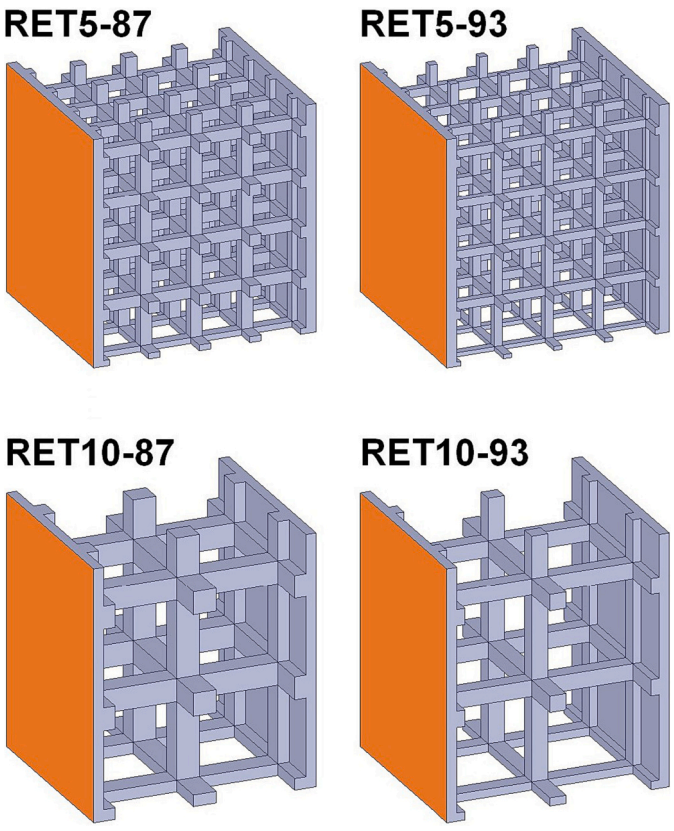

Fig. 10. Reticular structures considered in the thermal performance analysis (orange: heated surface).

to two relevant types of practical applications, namely, thermal control of intermittently operating devices and thermal energy storage, two different boundary conditions were adopted for the heated surface: an imposed heat flux condition and an imposed constant temperature condition of a few degrees above the phase change interval of each of the paraffin waxes. The initial temperatures T_{init} were in all cases a few degrees below the phase change interval so that all simulated transients encompassed the entire melting range. More in detail, the tests were carried out using the following boundary and initial conditions:

- imposed heat flux $HF = 10$ kW m^{-2} and $T_{init} = 34$ °C, 48 °C and 56 °C for RT42, RT55 and RT64HC paraffins, respectively;
- imposed constant temperature $T_{heat} = 46$ °C and $T_{init} = 34$ °C with RT42, $T_{heat} = 60$ °C and $T_{init} = 48$ °C with RT55, and $T_{heat} = 68$ °C and $T_{init} = 56$ °C with RT64HC.

Fig. 11 shows the time evolution of the heated surface temperature for all the structures and considered paraffins when imposed heat flux conditions are applied. The trends of the curves confirm what was previously observed, namely, that the RET5-87 structure provides the best control of the surface temperature, which is the lowest in all cases. The worst results are obtained with RET10-93, while the RET5-93 and RET10-87 structures have very similar intermediate behavior.

To give further physical insight into the investigated phenomena, an example of how the thermal field develops over time in the four structures considered in the case of the RT42 paraffin, with the imposed temperature boundary condition $T_{heat} = 46$ °C and initial temperature $T_{init} = 34$ °C, is given in Fig. 12, where the temperature maps on the lateral surfaces of repetitive portions of the considered geometries comprising four computational domains are displayed at four time instants. In the figure, it is possible to visually appreciate how much faster the thermal field develops in the case of the RET5-87 structure than in all the others. In particular, it is apparent that after 690 s the temperature for this structure is everywhere above the temperature of complete melting of the PCM, while for the others the process is significantly more behind. In any event, as could have been easily guessed, in all cases the melting occurs first in the vicinity of the metal parts with high thermal conductivity and only later at the more distant points because of the low thermal conductivity of the PCM; for this reason, the structures with the larger cell sizes are less effective. In all cases, the point with the lowest temperature turns out to be the one located approximately in the center of the furthest cell from the heated surface (hereafter referred to as point C), which is at a distance from the surface itself of 17.5 mm in RET5-87 and RET5-93 structures, and 15.0 mm in RET10-87 and RET10-93 structures.

Fig. 13 shows the time trends of the cold spot temperature T_C during the transients when the imposed temperature conditions are applied. It provides a fairly accurate idea of the PCM melting times with all the structures and paraffins considered. Again, we find confirmation that the highest melting rate is with the RET5-87 structure, that with RET10-93 the process is much slower, and that the RET5-93 and RET10-87 structures exhibit intermediate and very similar thermal performance.

Finally, Fig. 14 shows the trend in time of the stored thermal energy H per unit area of the heated surface, calculated as the time integral of the specific heat flux at the surface. The maximum is reached when the entire PCM is at the temperature set as a boundary condition. It can be clearly seen that, as an obvious consequence of the different effectiveness of the considered reticular structures in diffusing heat within the paraffin wax, the rate of energy accumulation is very different and is the highest in the case of the structure with lower porosity and smaller cells. However, the maximum thermal energy stored per square meter is attained with the composite structures with 93 % porosity because in this case the amount of PCM embedded in the reticular metal matrix is larger.

6. Conclusion

This paper reports the result of some experimental and numerical tests regarding the melting of three paraffin waxes, having different

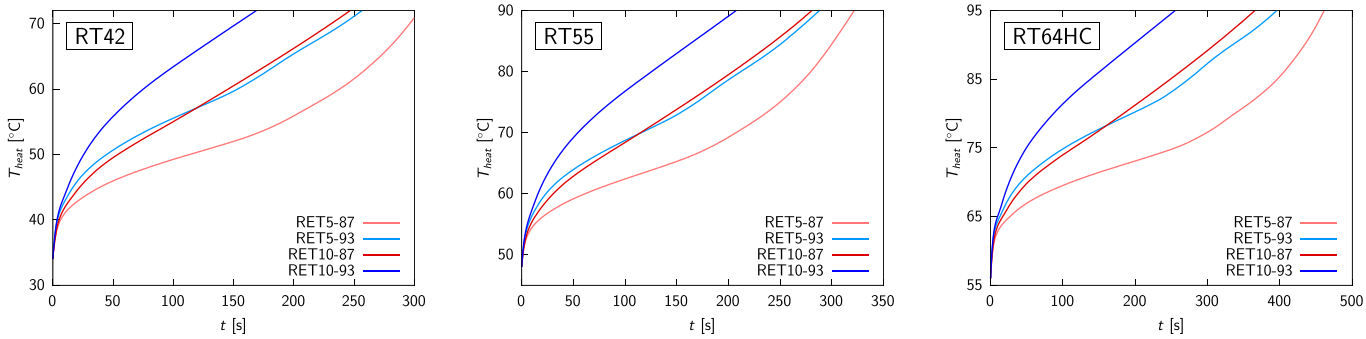

Fig. 11. Heated surface: time-temperature profiles for $HF = 10$ kW m^{-2}.

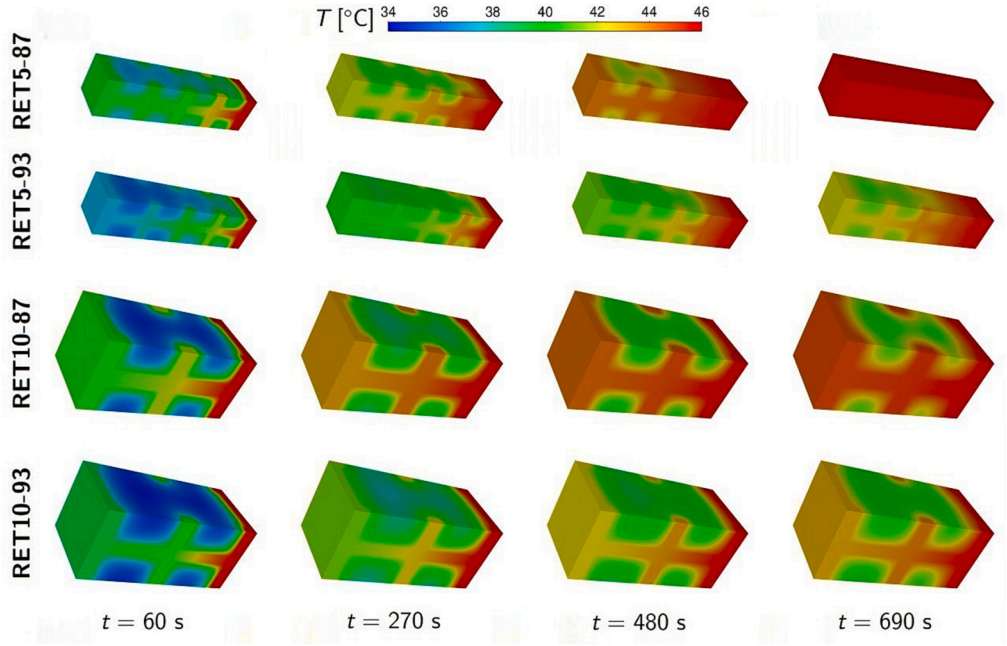

Fig. 12. Time evolution of the temperature distributions on the lateral surfaces of repetitive units of all the reticular structures for the RT42 wax, $T_{init} = 34°C$, and $T_{heat} = 46°C$.

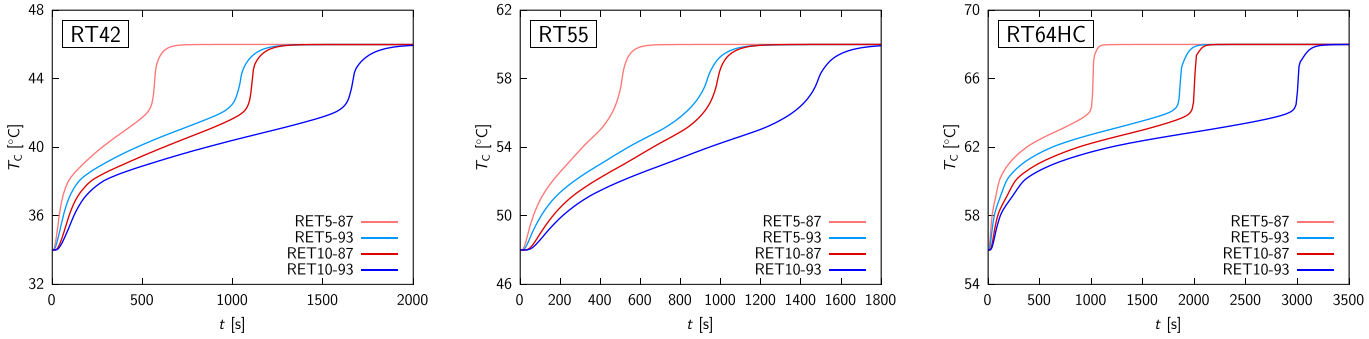

Fig. 13. Point C: time-temperature profiles for all the structures and PCMs with temperature boundary conditions.

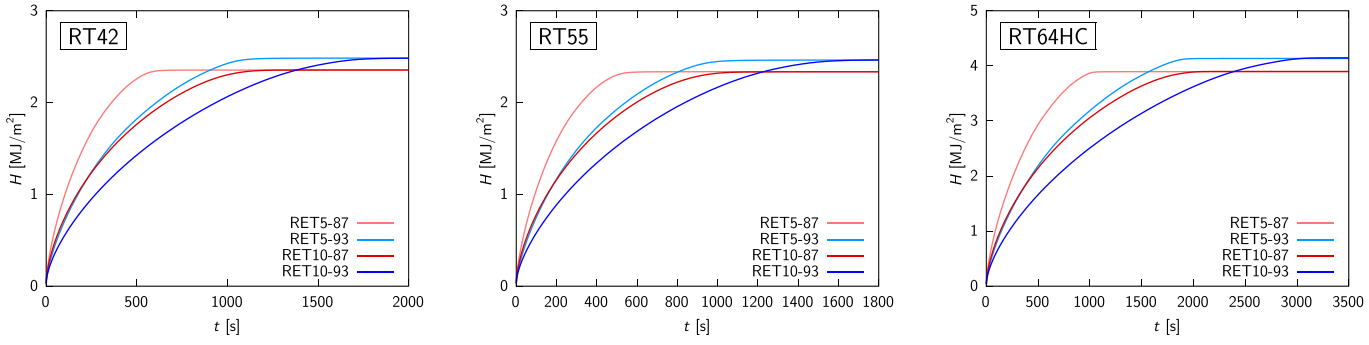

Fig. 14. Trend in time of the stored thermal energy H per unit area of the heated surface for temperature boundary conditions.

characteristic melting temperatures (42, 55, and 64 °C), embedded inside four reticular structures fabricated by additive manufacturing technology. The reticular structures have base cells of 5 mm and 10 mm, with porosities of 87% and 93%, and are made of aluminum alloy (AlSi10Mg). The samples were tested in an upright position and laterally heated by applying three heat fluxes (10, 15, and 20 kW m^{-2}).

All the experimental data were used to validate a numerical model to predict the behavior of the PCM-impregnated reticular structures. The numerical simulations, which were performed using ANSYS Fluent, were conducted on computational domains that only represent small repetitive portions of the test modules, thus allowing substantial savings in the computational time. The validation was carried out by a direct comparison between the numerical and experimental temperatures of the heated plate, as well as of the PCM, for each combination of reticular

structure, paraffin wax, and applied heat flux. The good agreement between numerical results and experimental data proves that this simplified model can be confidently used to assess the thermal performances of different structures and to carry out systematic studies aimed at optimizing the geometries of the metal matrices that can be used to increase the apparent thermal conductivity of PCM and improve process efficiency.

The main outcome of this work is the setup of the simplified numerical procedure, which was then validated and used to analyze the thermal performance of the same reticular structures and paraffins considered in the experiments, but with reference to ideal situations in which one of the surfaces of the layer comprising the metal matrix and PCM was kept adiabatic, while imposed specific heat flux or temperature boundary conditions were applied on the opposite surface. In fact, such boundary conditions may be deemed relevant with regard to situations where the considered structures could be used for thermal control of intermittently operating devices or for applications involving thermal energy storage.

The experimental and numerical results revealed that the effects of the geometrical parameters of the reticular structures on the heating process were such that, the effectiveness in diffusing heat into the PCM is greater if, for the same cell size, the porosity is smaller and if, for the same porosity, the cell size is smaller, i.e., the metal matrix is finer. Therefore, it is possible to conclude that, with all the paraffin waxes considered, the best overall thermal performance can be obtained with a metal matrix having a porosity of 87% and a cell size of 5 mm, which enables faster melting processes and better control of surface temperatures.

CRediT authorship contribution statement

Carlo Nonino: Conceptualization, Data curation, Formal analysis, Software, Validation, Writing – original draft. **Luisa Rossetto:** Funding acquisition, Writing – review & editing. **Andrea Diani:** Conceptualization, Investigation, Validation, Writing – review & editing.

Declaration of competing interest

The authors declare that they have no known competing financial interests or personal relationships that could have appeared to influence the work reported in this paper.

Data availability

Data will be made available on request.

Acknowledgements

The support of the MIUR through the PRIN Project 2017F7KZWS on this research is gratefully acknowledged. The LAMA FVG lab (Udine, Italy) is gratefully acknowledged for the 3D printing of the structures.

References

[1] H. Moon, K. Boyina, N. Miljkovic, W.P. King, Heat transfer enhancement of single-phase internal flows using shape optimization and additively manufactured flow structures, Int. J. Heat Mass Transf. 177 (2021), 121510.
[2] V. Papetti, P. Dimopoulos Eggenschwiler, A. Della Torre, G. Montenegro, A. Onorati, A. Ortona, G. Koltsakis, Instationary heat and mass transfer phenomena in additive manufactured open cell polyhedral structures for automotive catalysis, Chem. Eng. Sci. 234 (2021), 116448.
[3] D. Kong, Y. Zhang, S. Liu, Convective heat transfer enhancement by novel honeycomb-core in sandwich panel exchanger fabricated by additive manufacturing, Appl. Therm. Eng. 163 (2019), 114408.
[4] J.Y. Ho, K.C. Leong, T.N. Wong, Additively-manufactured metallic porous lattice heat exchangers for air-side heat transfer enhancement, Int. J. Heat Mass Transf. 150 (2020), 119262.
[5] H. Rastan, A. Abdi, B. Hamawandi, M. Ignatowicz, J.P. Meyer, B. Palm, Heat transfer study of enhanced additively manufactured minichannel heat exchanger, Int. J. Heat Mass Transf. 161 (2020), 120271.
[6] H. Moon, N. Miljkovic, W.P. King, High power density thermal energy storage using additively manufactured heat exchangers and phase change material, Int. J. Heat Mass Transf. 153 (2020), 119591.
[7] G. Righetti, G. Savio, R. Meneghello, L. Doretti, S. Mancin, Experimental study of phase change material (PCM) embedded in 3D periodic structures realized via additive manufacturing, Int. J. Therm. Sci. 153 (2020), 106376.
[8] A. Diani, L. Moro, L. Rossetto, Melting of paraffin waxes embedded in a porous matrix made by additive manufacturing, Appl. Sci. 11 (2021) 5396.
[9] M. Morciano, M. Alberghini, M. Fasano, M. Almiento, F. Calignano, D. Manfredi, P. Asinari, E. Chiavazzo, 3D printed lattice metal structures for enhanced heat transfer in latent heat storage systems, J. Energy Storage 65 (2023), 107350.
[10] S. Piacquadio, M. Schirp-Schoenen, M. Mameli, S. Filippeschi, K.-U. Schröder, Experimental analysis of the thermal energy storage potential of a phase change material embedded in additively manufactured lattice structures, Appl. Therm. Eng. 216 (2022), 119091.
[11] X. Hu, X. Gong, Experimental and numerical investigation on thermal performance enhancement of phase change material embedding porous metal structure with cubic cell, Appl. Therm. Eng. 175 (2020), 115337.
[12] W. Wu, X. Yang, G. Zhang, X. Ke, Z. Wang, W. Situ, X. Li, J. Zhang, An experimental study of thermal management system using copper mesh-enhanced composite phase change materials for power battery pack, Energy 113 (2016) 909–916.
[13] E. Lohse, G. Schmitz, Experimental analysis of regularly structured composite latent heat storages for temporary cooling of electronic components, Heat Mass Transf. 49 (11) (2013) 1565–1575.
[14] M. Reiswich, H. Brandt, M. Czupalla, Passive Thermal Control by Integration of Phase Change Material into Additively Manufactured Structures, Proceedings of 70th International Astronautical Congress, IAC 2019, 2019.
[15] Z.A. Qureshi, S.A.B. Al-Omari, E. Elnajjar, O. Al-Ketan, R.A. Al-Rub, Architected lattices embedded with phase change materials for thermal management of high-power electronics: a numerical study, Appl. Therm. Eng. 219 (2023), 119420.
[16] Z.A. Qureshi, S.A.B. Al-Omari, E. Elnajjar, O. Al-Ketan, R.A. Al-Rub, Nature-inspired triply periodic minimal surface-based structures in sheet and solid configurations for performance enhancement of a low-thermal-conductivity phase-change material for latent-heat thermal-energy-storage applications, Int. J. Therm. Sci. 173 (2022), 107361.
[17] Rubitherm Technologies GmBH Available online: https://www.rubitherm.eu/en/index.php/productcategory/organische-pcm-rt.
[18] K. Lafdi, O. Mesalhy, S. Shaikh, Experimental study on the influence of foam porosity and pore size on the melting of phase change materials, J. Appl. Phys. 102 (2007), 083549.
[19] J.W. Paek, B.H. Kang, S.Y. Kim, J.M. Hyun, Effective thermal conductivity and permeability of aluminum foam materials, Int. J. Thermophys. 21 (2000) 453.
[20] Z. Chen, D. Gao, J. Shi, Experimental and numerical study on melting of phase change material in metal foams at pore scale, Int. J. Heat Mass Transf. 72 (2014) 646–655.
[21] C. Zhao, M. Opolot, M. Liu, F. Bruno, S. Mancin, K. Hooman, Phase change behaviour study of PCM tanks partially filled with graphite foam, Appl. Therm. Eng. 196 (2021), 117313.
[22] ANSYS, Inc., ANSYS Fluent theory guide, Release 22/R2 (2022).
[23] A. Diani, C. Nonino, L. Rossetto, Melting of phase change materials inside periodic cellular structures fabricated by additive manufacturing: experimental results and numerical simulations, Appl. Therm. Eng. 215 (2022), 118969.
[24] K.K. Tamma, R.R. Namburu, Recent advances, trends and new perspectives formulations for applications to solidification problems via enthalpy-based finite element, Int. J. Numer. Methods Eng. 30 (1990) 803–820.